

Power Amplifiers With Frequency-Selective Matching Networks

José Antonio Estrada¹, Member, IEEE, José R. Montejo-Garai², Pedro de Paco, Member, IEEE, Dimitra Psychogiou³, Senior Member, IEEE, and Zoya Popović⁴, Fellow, IEEE

Abstract—In this article, we demonstrate a method for code-design of filtering matching networks for power amplifiers (PAs) with the desired frequency response, improved efficiency, and reduced footprint. The microwave transistor operates with high efficiency with a specific complex-impedance load, and this requires the development of a theory for filter matching network design with arbitrary complex-impedance ports. The formulation is first developed and then applied to a simple second-order filter and a fourth-order filter with cross couplings and transmission zeros and verified in the experiment. A single-stage high-efficiency 4.7-GHz, 4-W hybrid GaN filter-PA (FPA) within a sub-6-GHz 5G band is designed, built, and characterized. The port impedances are determined by load- and source-pull for an efficiency-power tradeoff. The measured performance shows a gain of 15 dB, PAE = 55% with 9% fractional bandwidth, and 10-dB rejection at 4.5 and 5 GHz. Comparison with a cascaded PA-filter circuit shows a 25% lower loss with the same rejection and a reduced footprint with the same rejection. A GaAs monolithic microwave integrated circuit (MMIC) FPA at 28 GHz (millimeter-wave 5G FR2 band) is also designed and measured with a second-order output matching filter, demonstrating 8-dB gain, 200 mW of output power, and PAE = 30% with a rejection of 8 dB at 26.5 and 29.6 GHz.

Index Terms—Ceramic, coaxial resonators, coupling matrix, 5G, GaAs, GaN, monolithic microwave integrated circuit (MMIC), power amplifiers (PAs), RF filters.

I. INTRODUCTION

POWER amplifier (PA) efficiency is an important parameter in RF front ends since the PA is often the dominant power consumption component. In high-efficiency PAs, the transistors are driven into saturation, resulting in linearity

Manuscript received June 23, 2020; revised July 31, 2020; accepted August 6, 2020. Date of publication September 14, 2020; date of current version January 5, 2021. This work was supported in part by the NSF SpeCEES Program under Grant ECCS-1731956 and in part by the Office of Naval Research under Award N00014-19-1-2487. This article is an expanded version from the 2020 IEEE MTT-S International Microwave Symposium (IMS) titled “Co-Designed High-Efficiency GaN Filter Power Amplifier,” Virtual Event, Aug. 4–Sep. 30, 2020. (Corresponding author: José Antonio Estrada.)

José Antonio Estrada, Dimitra Psychogiou, and Zoya Popović are with the Department of Electrical, Computer and Energy Engineering, University of Colorado at Boulder, Boulder, CO 80309 USA (e-mail: jose.estrada@colorado.edu).

José R. Montejo-Garai is with the Grupo de Electromagnetismo Aplicado, Information Processing and Telecommunications Center, Universidad Politécnica de Madrid, 28040 Madrid, Spain (e-mail: joseramon.montejo@upm.es).

Pedro de Paco is with the Department of Telecommunications and Systems Engineering, Universitat Autònoma de Barcelona, 08193 Barcelona, Spain.

Color versions of one or more of the figures in this article are available online at <https://ieeexplore.ieee.org>.

Digital Object Identifier 10.1109/TMTT.2020.3020097

0018-9480 © 2020 IEEE. Personal use is permitted, but republication/redistribution requires IEEE permission. See <https://www.ieee.org/publications/rights/index.html> for more information.

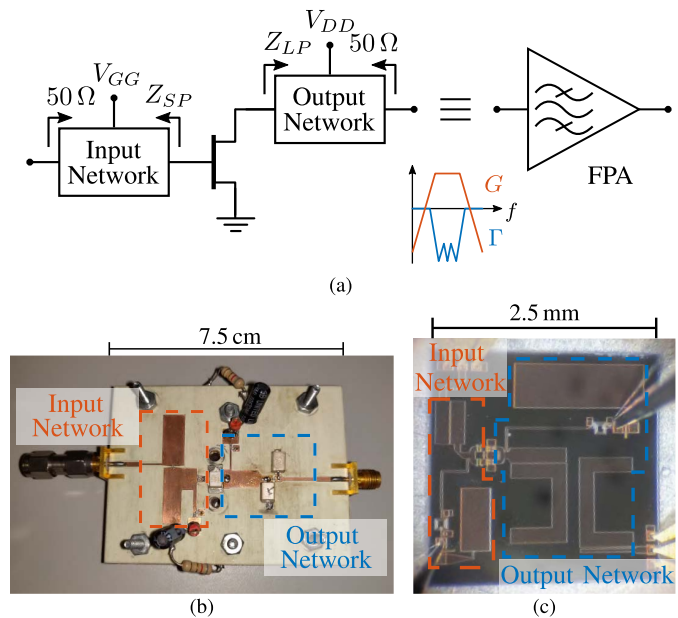


Fig. 1. (a) Block diagram of the FPA, where the input and output networks are codesigned fundamental matching, harmonic termination, stability, and bias networks, with a specific filter frequency response. (b) Hybrid implementation of an FPA designed for operation at a center frequency of 4.7 GHz (5G-FR1) with a 9% bandwidth. (c) MMIC implementation of an FPA designed for operation at a center frequency of 28 GHz (5G-FR2) with a 9% bandwidth.

degradation [1], [2], exhibited as both in-band and out-of-band distortion [3]. Both of these can be somewhat addressed with analog or digital predistortion (DPD) [4]–[6], and some band-limited DPD schemes can be used to simplify system complexity with sophisticated 5G signals [7]. In many cases, PAs require additional filtering at the output to satisfy spectral masks. For example, out-of-band nonlinearities, including those further from the signal up to harmonic frequencies, are addressed by filtering in [8]. As more capacity is required in wireless communication, features such as carrier aggregation make the problem of nonlinearities worse and filtering becomes more important [9]. Controlled filtering adjacent to an amplifier can also help with stability and provide an extra degree of freedom during the design [10]. Filters cascaded at the input and output of microwave amplifiers in RF front ends [11] increase the overall loss and size. Different applications favor either reduced loss, e.g., in high-power base-station transmitters [12] and in low-noise receivers [13] or reduced size in portable devices [14] or space applications [15].

Integration of the lossy matching network and filter can improve efficiency and reduce the size of a PA, as shown in Fig. 1. Here, the matching, harmonic terminations, bias, and stability networks (SNs) are all considered together and designed to have a specific filter-type frequency response, as shown in more detail in Fig. 2. Since transistors need to be matched to complex impedances for optimal operation, the first challenge is to establish a design method for complex terminations, rather than the real-valued source and load impedances that are used in standard filter design.

Previous efforts in this direction for amplifier design include [16] and [17], where the second- and third-order output PA filter networks are implemented with evanescent-mode (EVA) cavity resonators around 3 GHz. Both are narrowband [less than 3% fractional bandwidth (FBW)] with 10 W of output power, efficiencies around 70% and greater than 10 dB gain. The corresponding equations for filter design are shown for the specific cases of the second- and third-order all-pole transfer functions with only one complex terminated port. Guo *et al.* [18] extended the work in [16] by adding a source-to-load coupling, which allows two symmetric transmission zeros to be added to the frequency response.

Additional research in [19] presents an active $N+3$ coupling matrix that extends the work in [17] by generalizing to an n th order mainline waveguide filter while incorporating a transistor model for small-signal input conjugately matched amplifier design. This work is expanded in [20] to include a filter output match and in [21] to include the effect of gate–drain feedback and estimate the noise figure from the coupling matrix.

Here, we generalize the existing filter theory to include complex input and output impedances for the n th order filters with internal cross couplings. The initial work in [22] is extended both theoretically and experimentally. We extend the coupling matrix formulation and present an intuitive circuit-level treatment for complex-impedance ports. We show that a simple modification of the standard coupled-resonator filter design approach is valid for complex port impedances synthesized with traditional techniques for real loads. We then validate this theory with proof-of-concept second- and fourth-order

filters, as well as a hybrid filter-PA (FPA) at 4.7 GHz and a GaAs monolithic microwave integrated circuit (MMIC) FPA at 28 GHz, as shown in Fig. 1(b) and (c).

This article is outlined as follows. Section II presents the theoretical analysis for filter design with arbitrary complex-impedance loads at both the input and output, with cross couplings between resonators. Two passive filters validate the theory experimentally in Section III, which is then applied to the design of FPAs in Section IV. Starting from load–pull and source–pull impedances in 5G bands, a sub-6-GHz hybrid GaN PA and a 28-GHz GaAs MMIC PA are demonstrated and compared to published work in the conclusions of Section V.

II. ARBITRARY COMPLEX-IMPEDANCE FILTER DESIGN

The $N \times N$ coupling matrix concept was introduced by Atia *et al.* [22] and Atia and Williams [23]–[25] in a series of articles. In [26], the concept is extended to an $N + 2$ coupling matrix, which includes the source and load couplings. The matrix synthesis process is also extended to the case of matrices designed to operate with complex terminations. Very general examples of a fully canonical fourth-order asymmetric filter and a noncanonical fourth-degree asymmetric Chebyshev filter with two transmission zeros are given. In the first case, a direct comparison of the matrices designed for real and complex terminations shows that all the coupling values change. For the latter, it is shown that only the first and last resonators and the input and output couplings are affected by the change in terminating normalized impedances. This generalized coupling matrix synthesis procedure can be applied in principle to any case, but it does not give simple intuition or insight about the filter. Here, we prove that only the two elements next to the source and load need to be changed and provide the closed-form formulas that give the exact modification necessary to match the filter to the complex impedances of a transistor or for that matter any other complex-impedance component.

An n th order filter node diagram with no direct source-to-load coupling is shown in Fig. 3(a). The $N + 2$ coupling matrix ($[m_0]$) for such a filter is given by (1), as shown

$$[m_0] = \begin{bmatrix} 0 & m_{S1} & 0 & \cdots & \cdots & 0 & 0 \\ m_{S1} & m_{11} & m_{12} & \cdots & \cdots & m_{1n} & 0 \\ 0 & m_{12} & m_{22} & \cdots & \cdots & m_{2n} & 0 \\ \vdots & \vdots & \vdots & \ddots & & \vdots & \vdots \\ \vdots & \vdots & \vdots & & \ddots & m_{(n-1)n} & 0 \\ 0 & m_{1n} & m_{2n} & \cdots & m_{(n-1)n} & m_{nn} & m_{nL} \\ 0 & 0 & 0 & \cdots & 0 & m_{nL} & 0 \end{bmatrix} \quad (1)$$

$$[m] = [m_0] + [\Delta m] = \begin{bmatrix} 0 & m_{S1} & 0 & \cdots & \cdots & 0 & 0 \\ m_{S1} & m_{11} + \Delta m_1 & m_{12} & \cdots & \cdots & m_{1n} & 0 \\ 0 & m_{12} & m_{22} & \cdots & \cdots & m_{2n} & 0 \\ \vdots & \vdots & \vdots & \ddots & & \vdots & \vdots \\ \vdots & \vdots & \vdots & & \ddots & m_{(n-1)n} & 0 \\ 0 & m_{1n} & m_{2n} & \cdots & m_{(n-1)n} & m_{nn} + \Delta m_n & m_{nL} \\ 0 & 0 & 0 & \cdots & 0 & m_{nL} & 0 \end{bmatrix} \quad (2)$$

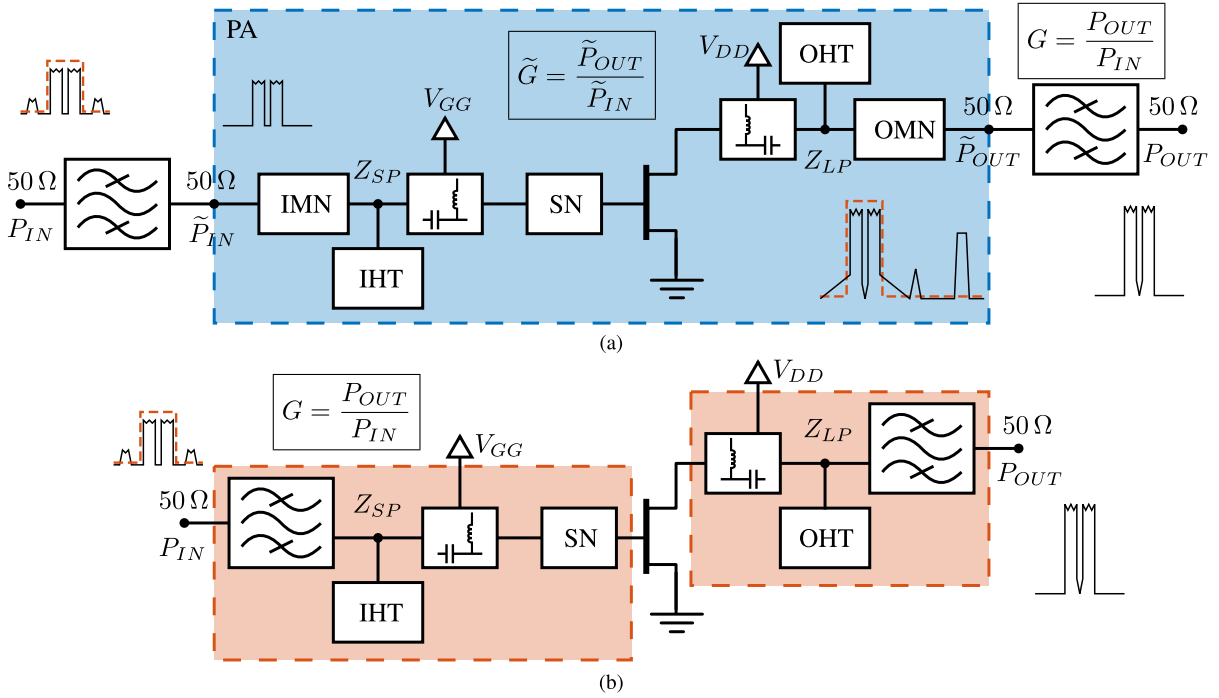


Fig. 2. (a) Block diagram of a PA cascaded with filters at input and output, where the shaded area shows the PA alone. The PA consists of an IMN, input harmonic termination (IHT), input bias tee, an SN, a transistor, output bias tee, output harmonic termination (OHT), and OMN. (b) Block diagram of the FPA, where the input and output filters are the codesigned IMFs. The shaded input and output networks correspond to the ones shown in Fig. 1(a).

at the bottom of the previous page. The frequency response of this filter is designed in normalized space (1- Ω reference impedance and $\omega = 1$ normalized angular frequency), where it does not depend on the source and load impedances. The circuit elements in Fig. 3(b) can be obtained from the coupling matrix $[m_0]$ for a given center frequency, bandwidth, and port resistances, following the procedure in [26] and [27]. Note that the coupling coefficients M_{ij} are denormalized. The input and output port impedances in Fig. 3(b) are complex and correspond to the transistor impedances in an amplifier that maximize gain, efficiency, and so on. For a PA, for example, the input impedance of the filter matching network is found through load-pull and is a complex impedance that is typically a tradeoff between efficiency and power. The goal of the analysis shown below is to develop a method that allows a standard filter design to be applied to ports with predetermined amplifier complex impedances.

We refer to the filter described by $[m_0]$ as the “original design,” which can be obtained using any coupled-resonator synthesis technique [26], [27] and is traditionally designed for real-valued port impedances. A new coupling matrix, given by (2), as shown at the bottom of the previous page, is created by adding variations Δm_1 and Δm_n in the m_{11} and m_{nn} terms, respectively. The normalized input admittance of the filter is

$$y_{in} = \frac{m_{S1}^2}{s + j(m_{11} + \Delta m_1) + h_L(s, [m_0], \Delta m_n, z_L)} \quad (3)$$

where $h_L(s, [m_0], \Delta m_n, z_L)$ is the equivalent admittance seen by the first resonator looking into the rest of the terminated filter and depends on the topology of the filter.

The reactance of the last resonator is always in parallel with the admittance of the load transformed by the last inverter, resulting in

$$\begin{aligned} y_n &= j(m_{nn} + \Delta m_n) + m_{nL}^2 z_L \\ &= jm_{nn} + (j\Delta m_n + m_{nL}^2 z_L) \end{aligned} \quad (4)$$

where y_n is the admittance of the n th resonator in parallel with the inverted load. From (3) and (4), the dependence of the input admittance on Δm_n and z_L is contained in y_n . To shorten the derivation, we enforce independence of y_{in} on Δm_n and later show that this condition is equivalent to the simultaneous conjugate match. This produces

$$\begin{aligned} j\Delta m_n + m_{nL}^2 z_L &= K_L \\ z_L &= \frac{K_L}{m_{nL}^2} - j\frac{\Delta m_n}{m_{nL}^2} \end{aligned} \quad (5)$$

where K_L is an auxiliary parameter that, without loss of generality, can be used to normalize the real part of z_L . This leads to

$$K_L = m_{nL}^2 \quad (6)$$

consequently making h_L independent of z_L and Δm_n as long as condition (5) is held. Namely,

$$\begin{aligned} h_L(s, [m_0], \Delta m_n, z_L) &= h_L(s, [m_0], y_n) \\ &= h_L(s, [m_0], m_{nn}, K_L) \\ &= h_L(s, [m_0], m_{nn}, m_{nL}^2) \\ &= h_L(s, [m_0]) \end{aligned} \quad (7)$$

because m_{nn} and m_{nL} are contained within $[m_0]$.

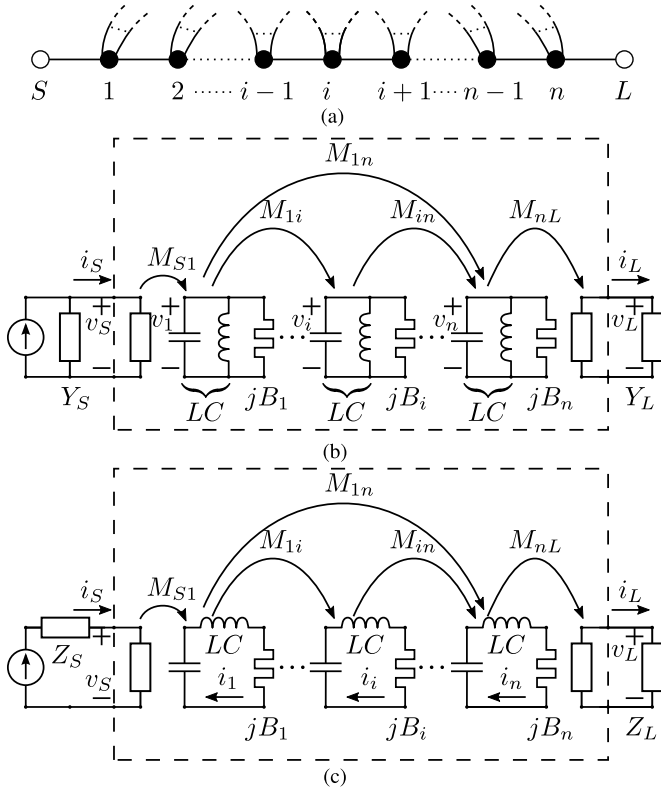


Fig. 3. (a) General filter node diagram for an n th order filter where nodes (resonators) i can connect to $n-1$ nodes, while nodes 1 and n can connect to n resonators. The exceptions are nodes S and L , which only connect to nodes 1 and n , respectively. Circuit representation with (b) parallel and (c) series resonators.

The input impedance is obtained from (3) and (7) as

$$\begin{aligned} z_{\text{in}} &= \frac{1}{y_{\text{in}}} \\ &= \frac{h_L(s, [m_0]) + s + jm_{11} + j\Delta m_1}{m_{S1}^2} \\ &= \left[\frac{h_L(s, [m_0]) + s + jm_{11}}{m_{S1}^2} \right] + j \frac{\Delta m_1}{m_{S1}^2} \end{aligned} \quad (8)$$

given that the load impedance is

$$z_L = 1 - j \frac{\Delta m_n}{m_{nL}^2} = 1 + jx_L. \quad (9)$$

The output impedance of the filter can be similarly derived as

$$z_{\text{out}} = \left[\frac{h_S(s, [m_0]) + s + jm_{nn}}{m_{nL}^2} \right] + j \frac{\Delta m_n}{m_{nL}^2} \quad (10)$$

given that the source impedance is

$$z_S = 1 - j \frac{\Delta m_1}{m_{S1}^2} = 1 + jx_S. \quad (11)$$

The terms in brackets in (8) and (10) do not explicitly depend on the resonator variations Δm_1 and Δm_n and are the frequency responses of a filter designed to work with resistive terminations, which we refer to as the ‘‘original design’’ ($\Delta m_1 = \Delta m_n = 0$). In band, these terms are very close or equal to unity (at the poles), indicating a good match. The Appendix shows the proof that the frequency

response of the reflection coefficient of a filter terminated in the complex impedances (9) and (11) is exactly that of the resistively terminated original filter design.

The reactive part of the input and output port impedances can then be controlled by detuning the input or output resonators, 1 and n , respectively, while maintaining the same filter response. The real part of the port impedance remains normalized to the port resistance, and the necessary modification of the resonators for conjugate matching can be obtained from (8)–(11) as

$$\Delta m_1 = -x_S m_{S1}^2 = -\frac{X_S}{R_S} m_{S1}^2 \quad (12)$$

$$\Delta m_n = -x_L m_{nL}^2 = -\frac{X_L}{R_L} m_{nL}^2 \quad (13)$$

where X_S and X_L are the reactive parts of the source and load impedances, respectively, while R_S and R_L are the real parts and are also the normalizing resistances of the input and output ports, respectively.

This derivation works for parallel resonator topologies where the coupling matrix represents an admittance matrix (node equation formulation of the coupling matrix [27]). For the series resonator case (loop equation formulation of the coupling matrix [27]) shown in Fig. 3(c), the coupling impedance matrix variation terms can be similarly derived as

$$\Delta m_1 = -b_S m_{S1}^2 = -\frac{B_S}{G_S} m_{S1}^2 \quad (14)$$

$$\Delta m_n = -b_L m_{nL}^2 = -\frac{B_L}{G_L} m_{nL}^2 \quad (15)$$

where B_S and B_L are the reactive parts of the source and load admittances, respectively, while G_S and G_L are the real parts and are also the normalizing conductances of the input and output ports, respectively. It is worth noting that the frequency shift in the resonators is the same in the two cases, but with a different sign, since

$$\frac{B_S}{G_S} = -\frac{X_S}{R_S}. \quad (16)$$

A. Circuit-Level Analysis

Knowing that only the first and last resonators are modified, a simple and intuitive circuit analysis gives the same results as the coupled-resonator filter theory. Fig. 4(a) shows the low-pass representation of a resonator at one end of a filter and the inverter that couples that resonator to a resistive load. Fig. 4(b) shows the modified circuit where the resonator is altered by adding a frequency-invariant reactance (FIR) B_0 , which shifts the center frequency of the resonator. The equivalent input admittances are

$$Y_1 = j\omega C + Z_0 J_1^2 \quad (17)$$

$$Y_2 = jB_0 + j\omega C + (R + jX) J_2^2. \quad (18)$$

Equating these and solving for B_0 and J_2 , we obtain the modified values that will conserve filter performance

$$B_0 = -\frac{X}{R} Z_0 J_1^2 \quad (19)$$

$$J_2 = \pm J_1 \sqrt{\frac{Z_0}{R}}. \quad (20)$$

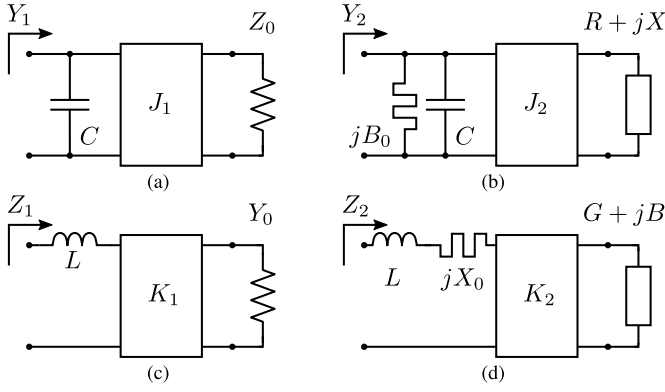


Fig. 4. Low-pass representation of an edge resonator, inverter, and termination for (a) parallel case and real termination, (b) parallel case and complex termination, (c) series case and real termination, and (d) series case and complex termination.

If we follow the same approach as in the previous part and make the real part equal to the original resistance ($R = Z_0$), it can be seen that the inverter value remains unchanged within a sign, $J_2 = J_1$, and the FIR value is given by

$$B_0 = -XJ_1^2 \quad (21)$$

which is analogous with (12) and (13).

Similarly, a filter with series resonators has the following equivalent impedances:

$$Z_1 = j\omega L + Y_0 K_1^2 \quad (22)$$

$$Z_2 = jX_0 + j\omega L + (G + jB)K_2^2 \quad (23)$$

which can be combined to find the new FIR X_0 and impedance inverter K_2 as

$$X_0 = -\frac{B}{G}Y_0 K_1^2 \quad (24)$$

$$K_2 = \pm K_1 \sqrt{\frac{Y_0}{G}}. \quad (25)$$

If $G = Y_0$, the following is obtained:

$$X_0 = -BK_1^2 \quad (26)$$

which is analogous to (14) and (15).

III. FILTER IMPLEMENTATIONS WITH COMPLEX PORTS

To verify the theory, we show two complex-to-complex impedance microstrip filter implementations: a second-order all-pole filter and a fourth-order elliptical filter, both Chebyshev type. They use the same 762- μm -thick Rogers 4350B substrate with 35- μm -thick copper traces and ground plane.

A. Second-Order Filter Example

A simple microstrip filter using quarter-wave inverters and half-wave resonator is designed for $Z_S = (35 - j10) \Omega$ and $Z_L = (60 + j15) \Omega$. The filter is a second-order all-pole

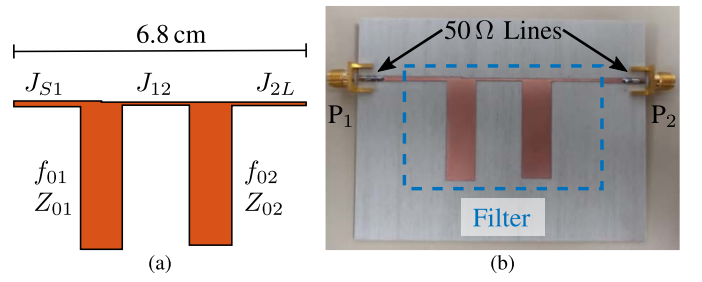


Fig. 5. (a) Layout and (b) photograph of the second-order filter. The dashed line indicates the position of the reference planes to which the 50- Ω line sections are deembedded using the through-reflect-line (TRL) calibration.

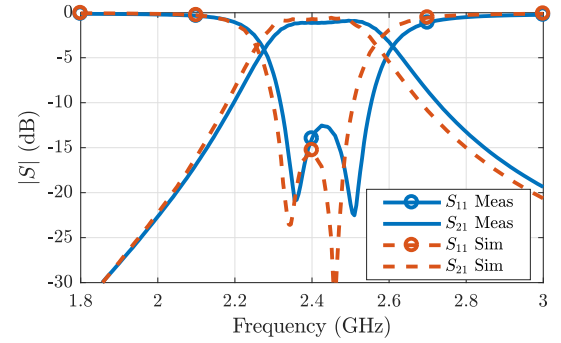


Fig. 6. Simulation and measurement results for the second-order Chebyshev microstrip filter seen in Fig. 5 with complex port impedances Z_S and Z_L . The measurement is performed in a 50- Ω environment and referenced to the complex port impedances in postprocessing.

Chebyshev type with a return loss $RL = 15$ dB, represented by the admittance coupling matrix

$$[m_0] = \begin{bmatrix} 0 & 1.0369 & 0 & 0 \\ 1.0369 & 0 & 1.2868 & 0 \\ 0 & 1.2868 & 0 & 1.0369 \\ 0 & 0 & 1.0369 & 0 \end{bmatrix} \quad (27)$$

which after modification for the complex-impedance loading using (12) and (13), becomes

$$[m] = \begin{bmatrix} 0 & 1.0369 & 0 & 0 \\ 1.0369 & 0.3072 & 1.2868 & 0 \\ 0 & 1.2868 & -0.2688 & 1.0369 \\ 0 & 0 & 1.0369 & 0 \end{bmatrix} \quad (28)$$

and this matrix is referenced to the real part of the port impedances ($z_{0i} = r_i$). The filter response is centered at $f_0 = 2.4$ GHz with 8% FBW. Fig. 5 shows the layout and photograph of the fabricated device.

This filter was designed using Cadence AWR for circuit and full-wave electromagnetic (EM) simulations (Axiem). The measured frequency response is compared to the simulations in Fig. 6, where the port impedances are the complex values previously specified. Fig. 7 shows the complex reflection coefficients at the filter ports when it is terminated in the design complex impedances. It can be seen that the impedances looking into the filter are conjugately matched to $Z_S = (35 - j10) \Omega$ and $Z_L = (60 + j15) \Omega$ in the passband (loop).

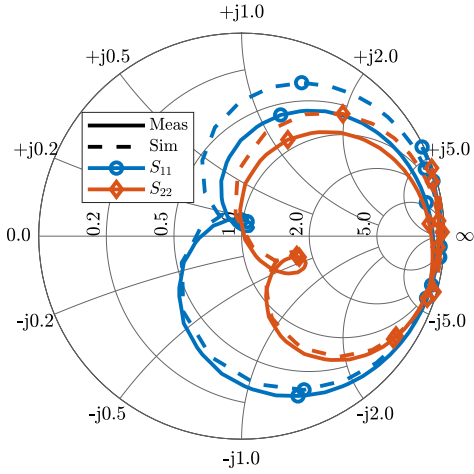


Fig. 7. Simulated and measured S_{11} and S_{22} for the second-order filter, from Fig. 5, terminated in Z_S and Z_L , plotted from 1.8 to 3 GHz. The measurement is performed in a $50\text{-}\Omega$ environment and referenced to the complex port impedances in postprocessing.

B. Fourth-Order Filter Example

The filter is a fourth-order elliptical Chebyshev type with two transmission zeros at $s_{1,2} = \pm j1.9$ (normalized angular frequency) and $RL = 20$ dB. Fig. 8(a) shows the node diagram for this filter where the original coupling matrix is

$$[m_0] = \begin{bmatrix} 0 & 1.02 & 0 & 0 & 0 & 0 \\ 1.02 & 0 & 0.86 & 0 & -0.19 & 0 \\ 0 & 0.86 & 0 & 0.78 & 0 & 0 \\ 0 & 0 & 0.78 & 0 & 0.86 & 0 \\ 0 & -0.19 & 0 & 0.86 & 0 & 1.02 \\ 0 & 0 & 0 & 0 & 1.02 & 0 \end{bmatrix}. \quad (29)$$

The filter is centered at $f_0 = 2.4$ GHz with 7.5% FBW. The port impedances are $Z_S = (25 - j10)\ \Omega$ and $Z_L = (80 + j20)\ \Omega$, and the modified coupling matrix is

$$[m_0] = \begin{bmatrix} 0 & 1.02 & 0 & 0 & 0 & 0 \\ 1.02 & -0.42 & 0.86 & 0 & -0.19 & 0 \\ 0 & 0.86 & 0 & 0.78 & 0 & 0 \\ 0 & 0 & 0.78 & 0 & 0.86 & 0 \\ 0 & -0.19 & 0 & 0.86 & 0.26 & 1.02 \\ 0 & 0 & 0 & 0 & 1.02 & 0 \end{bmatrix}. \quad (30)$$

The filter is shown in Fig. 8, where the couplings between the resonators are realized by adjusting the proximity (d_{ij}) between them. Resonators R_2 and R_3 are identical and resonate at the center frequency, whereas R_1 and R_4 are detuned according to (14) and (15) resulting in a higher resonant frequency (2.438 GHz) for the first resonator and a lower resonant frequency (2.377 GHz) for the last. Fig. 8 also shows a photograph of the fabricated filter and the layout.

The filter measured scattering parameters are compared to simulated ones in Fig. 9, where the four poles and two transmission zeros can be seen. Fig. 10 shows the input and output reflection coefficients of the filter when terminated in Z_S and Z_L . Variation from simulations is due to the fabrication tolerances and high sensitivity to filter dimensions, which leads to small shifts in the operating impedances, center frequency, and FBW.

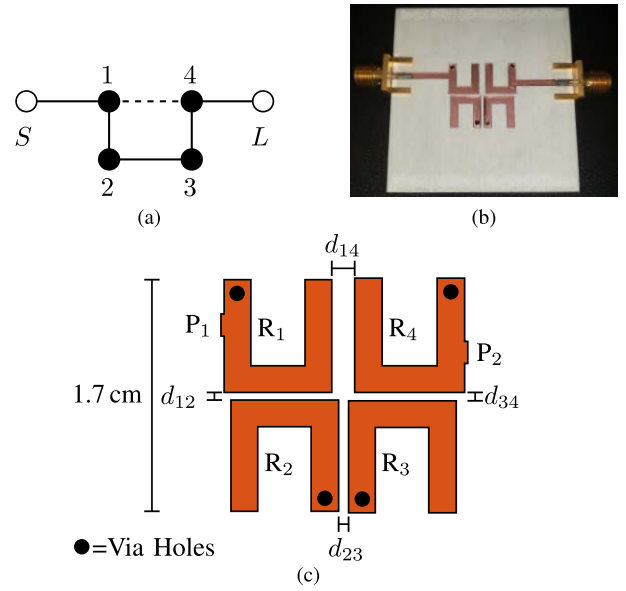


Fig. 8. Fourth-order elliptical microstrip filter. (a) Node diagram. (b) Photograph. (c) Layout.

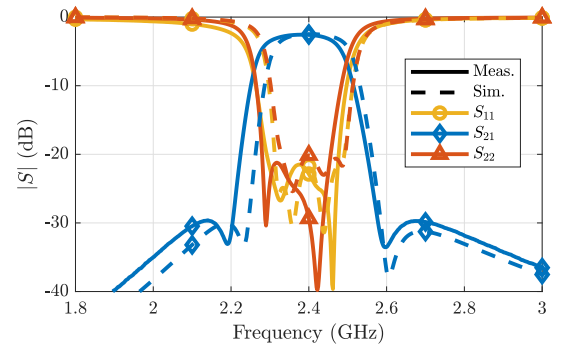


Fig. 9. S-parameters for the fourth-order microstrip filter. The simulated design works with a source impedance of $25 - j10\ \Omega$ and load impedance of $80 + j20\ \Omega$. The fabricated filter impedances are shifted to $25 - j5\ \Omega$ and $76 + j14\ \Omega$ for the source and load, respectively.

IV. FPA EXPERIMENTAL DEMONSTRATIONS

Two FPAs are designed for operation in the sub-6-GHz (FR1) and millimeter-wave (FR2) ranges of the 5G technical specification [28] utilizing filters as the matching networks, as shown in Figs. 1(a) and 2. The sub-6-GHz design is centered at 4.7 GHz with 36-dBm output power and is implemented as a hybrid circuit with a packaged GaN device. The millimeter-wave amplifier is a GaAs MMIC with a center frequency of 28 GHz with an output power of 23 dBm.

A. Hybrid 4.7-GHz GaN FPA

The fabricated hybrid FPA can be seen in Fig. 11. Due to the low Q -factor of microstrip resonators, and large impact of the output matching network (OMN) loss on PA efficiency [29], we use ceramic coaxial resonators ($Q = 700$, manufactured by T-Ceram) in the output matching filters. These have a dielectric constant of 20 and are custom made to work at the specific frequencies necessary for the design. The PA is designed

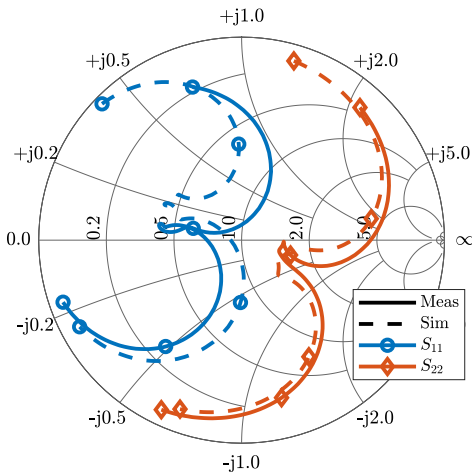


Fig. 10. Complex input and output reflection coefficients of the fourth-order filter from Fig. 8, plotted from 2.2 to 2.6 GHz.

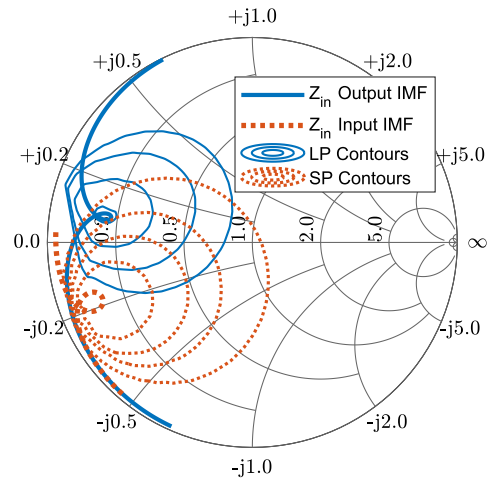


Fig. 12. Simulated IMF responses overlaid with 4.7-GHz load-pull and source-pull contours for Qorvo’s T2G6000528-Q3 GaN transistor. IMF responses are plotted from 3.4 to 6 GHz.

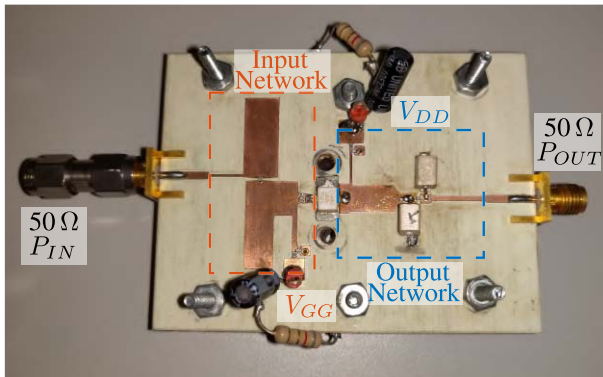


Fig. 11. Photograph of the hybrid GaN FPA designed for operation at a center frequency of 4.7 GHz with a 9% bandwidth.

around Qorvo’s T2G6000528-Q3 GaN packaged transistor and is simulated using Cadence AWR’s harmonic balance for the nonlinear simulations with a Modelithics nonlinear transistor model. The substrate is Rogers 4350B with a relative permittivity of $\epsilon_r = 3.75$ and a thickness of $762 \mu\text{m}$ and with $35\text{-}\mu\text{m}$ copper metallization.

The impedance matching filters (IMFs) at the input and output are designed to load the transistor with impedances for an efficiency and output power compromise. The fundamental impedances of the filters and harmonic terminations [30] are found using load-pull harmonic balance simulations, and Fig. 12 shows the load-pull and source-pull contours. It is worth noting that when the device impedance is highly reactive and close to the edge of the Smith chart such as the source-pull contours shown in Fig. 12, the matching becomes more complicated due to the Bode-Fano limit.

The IMFs are designed to have a second-order Chebyshev-type response with $RL = 15 \text{ dB}$ using the coupling matrix in (27). Both IMFs have a center frequency of 4.7 GHz and 9% FBW. They use open half-wavelength resonators and quarter-wavelength inverters at the input and output. The coupling between the resonators is implemented with a capacitor. The negative capacitances in the π -network inverter are accounted

for by a corresponding frequency shift in the resonators. The inverter also serves as the dc block in the transistor biasing network.

The modeling of the transition through the resonator tab in the output filter is essential. Here, it is modeled as a three-port network by 3-D EM simulations in Ansys HFSS [finite element method (FEM)], as shown in Fig. 13(a). A comparison of the simulation with and without including the geometry of the tab is given in Fig. 13b, showing the importance of accurate modeling of parasitic and propagation effects in this transition. The open end of the resonator is also characterized using the 3-D simulation and is very close to an ideal open circuit, as expected due to the high permittivity of the dielectric. Finally, the harmonic terminations are implemented with a shorted (grounded capacitor) stub that also serves as an RF choke for dc biasing of the gate and drain.

Small-signal measurements (see Fig. 14) show that the FPA exhibits a filter response in both gain and input reflection coefficient (Γ_{IN}). Fig. 15 shows the large-signal performance of the FPA at the peak-PAE power output (P_{OUT}). The measured PAE for the FPA at the center and the edges of the band is shown in Fig. 16. The PAE reaches 55% at 4.7 GHz with a saturated gain of 13.7 dB. The small discrepancies between simulations and measurements are attributed to fabrication tolerances in the PCB milling process, as well as the imperfect transistor nonlinear model.

B. GaAs MMIC 28-GHz FPA

The design procedure is next validated with a GaAs MMIC implementation in the WIN Semiconductor 150-nm GaAs PIH1-10 enhancement-mode HEMT process [see Fig. 17(a)]. The active device is an $8 \times 75 \mu\text{m}$ HEMT accomplished by combining two $4 \times 75 \mu\text{m}$ devices with a via between them for improved thermal performance. As in the hybrid design, the gate and drain impedances to be presented to the device are determined from load-pull simulations using the manufacturer-provided nonlinear model and EM-simulated manifolds.

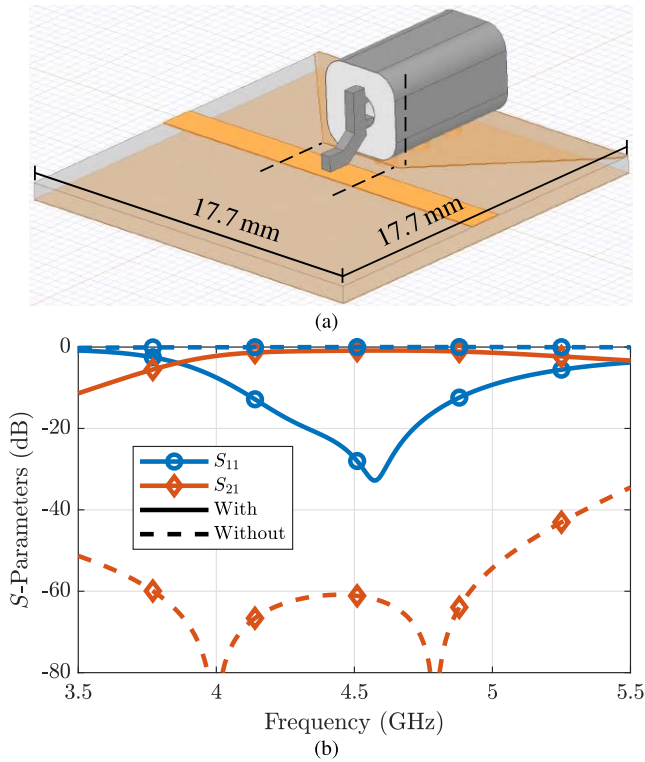


Fig. 13. (a) Resonator tab transition simulation model (HFSS) showing the deembedding planes for the three-port network. (b) Comparison of output IMF performance with and without modeling the tab transition.

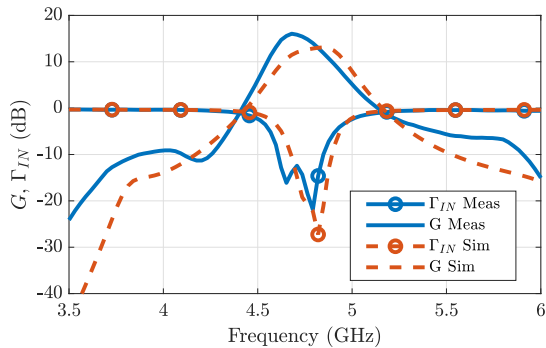


Fig. 14. Measured and simulated small-signal gain and input match of the FPA from Fig. 1.

The input matching network (IMN) is implemented with a compact coupled-line section, providing a dc block [31]. The output IMF is designed using the theory presented earlier with the same coupling matrix as given in (27), resulting in a second-order Chebyshev filter with $RL = 15$ dB. The center frequency of this filter is 28 GHz and the FBW is 5%. The resonators in the IMF are designed for high Q -factor using thick metal layers and varying resonator dimensions within the allowed MMIC process range. Careful choice of widths of the resonator lines and coupling section lengths minimizes the insertion loss and results in high efficiency and output power. The output coupled-resonator IMF provides a dc block for the drain bias. The RF choke and harmonic terminations are also codesigned following the concept from Fig. 2 and

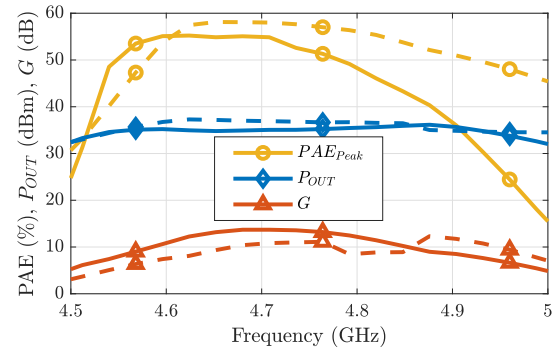


Fig. 15. Hybrid GaN FPA large-signal simulations and measurements as a function of frequency, where the dashed lines represent simulations. The efficiency, output power, and gain are all given at the peak efficiency point for all frequencies.

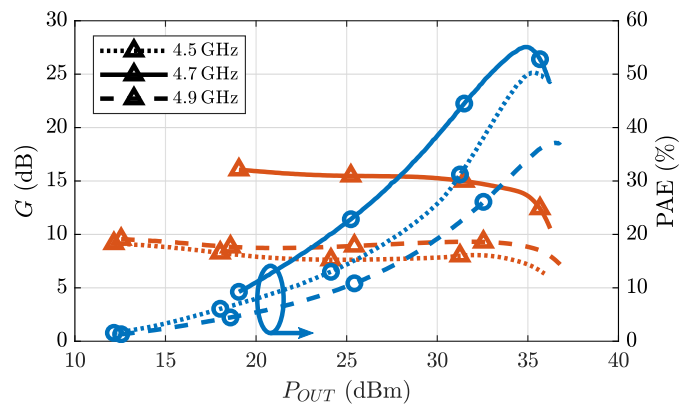


Fig. 16. Measured PAE as a function of P_{OUT} for the hybrid GaN FPA at the center and edges of the band.

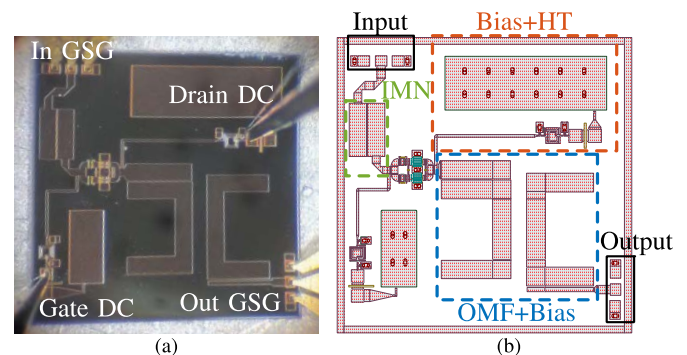


Fig. 17. (a) Photograph and (b) layout of the GaAs MMIC FPA. The die size is $2.5 \text{ mm} \times 2.5 \text{ mm}$.

with a grounded capacitor shorted stub at the operating frequency, as in the case of the hybrid FPA. Fig. 17(b) shows the layout and highlights the IMN, output IMF, and output biasing/harmonic terminations.

The MMIC FPA is measured on-wafer with a two-tier coaxial power and S-parameter calibration, followed by an SOLT on-wafer calibration. Fig. 18 shows the simulated and measured S-parameters of the amplifier showing agreement. It is worth noting that although the IMF is presenting the appropriate impedance to the transistor output for

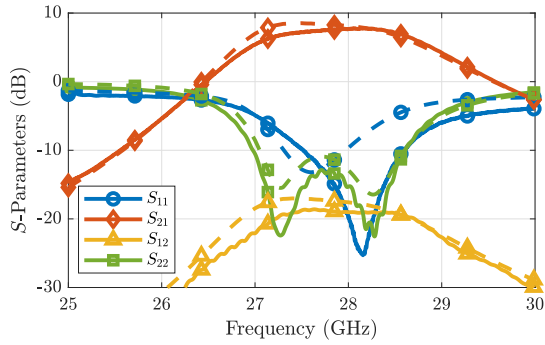


Fig. 18. Measured (solid line) and simulated (dashed line) S-parameters of the MMIC FPA from Fig. 17. All measured parameters track the simulated ones very closely.

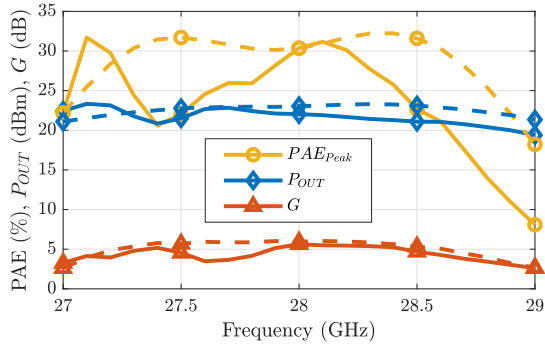


Fig. 19. MMIC FPA large-signal simulations and measurements as a function of frequency, where the dashed traces represent simulations. All traces are plotted at the point of peak PAE.

maximizing PAE, this is not a conjugate match and results in $|S_{22}| < -15$ dB not being met across the whole band. A frequency 400-MHz ($<1.5\%$) shift in S_{11} affects the gain at the lower end of the band.

Fig. 19 shows the measured and simulated large-signal performance of the MMIC FPA, once again showing agreement between measurement and simulation. The efficiency, output power, and gain are all given at the peak efficiency point for all frequencies. The decrease in measured small-signal gain compared to simulations from Fig. 18 of about 2 dB near 27.6 GHz, points to a possible decrease in PAE in large-signal operation. This is seen in the measurements in Fig. 19, where there is a dip in PAE around 27 GHz. This is likely due to a frequency shift in the response as well as the suboptimal thermal environment, as the MMIC was measured directly on the chuck of the probe station without additional thermal management which in turn typically reduces the gain. Finally, Fig. 20 shows the gain and PAE versus output power measured at three different frequencies.

V. CONCLUSION AND DISCUSSION

In this article, we present a method for codesigning filtering matching networks and PAs with the desired frequency response, improved efficiency, and reduced footprint. In order to implement this type of codesign, we developed a theory for simple design of filters with arbitrary impedance terminations, using the coupling matrix technique for coupled-resonator

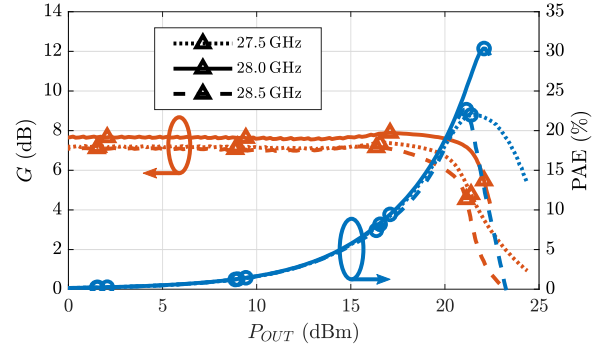


Fig. 20. Measured PAE as a function of P_{OUT} for the GaAs MMIC FPA at three different frequencies in the band.

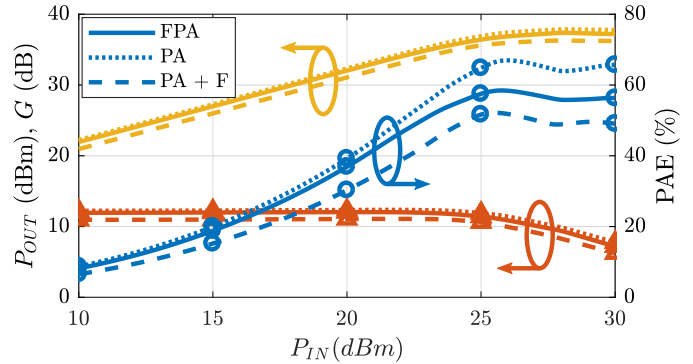


Fig. 21. Simulation comparison between the designed FPA and a PA where the OMN is made with a more traditional stub matching and that same PA cascaded with a filter designed in the same way as the one in the FPA but using $50\ \Omega$ ports on both sides. The footprint of the FPA is reduced by approximately 20% when compared to a cascaded PA and filter.

filters as well as a simplified circuit-based technique. The constraint in this general method is that only internal cross couplings between the resonators are allowed. The complex-impedance port formulation is first applied to a simple second-order filter and a fourth-order filter with cross couplings and transmission zeros. Two filters are implemented in microstrip at 2.4 GHz with all-pole and elliptical response, both with different complex impedances on the two ports. The filter design and simulations agree well with experiments, validating the theory.

The approach is then applied to a single-stage high-efficiency 4.7-GHz, 4-W hybrid GaN FPA within a sub-6-GHz 5G band. The measured performance shows a gain of 15 dB, PAE = 55% with 9% FBW, and 10-dB rejection at 4.5 and 5 GHz. Scaling to the millimeter-wave 5G band, a GaAs MMIC FPA at 28 GHz is also demonstrated with 8-dB gain, 200 mW of output power, and PAE = 30% with a rejection of 8 dB at 26.5 and 29.6 GHz. Fig. 21 shows a simulation comparison of the 4.7-GHz microstrip FPA with a PA designed with the same load-pull impedance for a $50\text{-}\Omega$ termination, cascaded with a filter with the same exact frequency response, topology, and implementation as the OMF in the FPA for a fair comparison.

A comparison of the state-of-the-art in co-designed filters and amplifiers with arbitrary complex impedances is shown in Table I. Some of the examples in the table are general

TABLE I

COMPARISON OF FPA WORK. * THEORY ALLOWS n TH ORDER DESIGNS. † ONLY CROSS COUPLING IS THE SOURCE-TO-LOAD ONE. ‡ THEORY ONLY ALLOWS INTERNAL CROSS COUPLINGS

Ref.	Order	Cross Couplings	Complex Ports	Resonator Technology	Amplifier Type	f_0 (GHz)	FBW (%)	G (dB)	P_{out} (dBm)	PAE (%)
[32]	2	-	No-O	Microstrip	Hybrid MOSFET PA	2.6	3.8	14.3	42.5	46
[8]	4	-	No-O	Microstrip	Hybrid GaN PA	2	20	16.2	40.5	62
[16]	2	No	Yes-O	EVA Cavity	Hybrid GaN PA	3	3	> 10	40	68
[17]	3	No	Yes-O	EVA Cavity	Hybrid GaN PA	3.1	1.7	15.5	40	67
[18]	2	Yes†	Yes-O	Coaxial Cavity	Hybrid GaN PA	2.4	11	18.2	41	71
[19]	2*	No	Yes-I	Rectangular Cavity	Hybrid GaAs GS	10	5	11.7	-	-
[20]	2*	No	Yes-IO	Rectangular Cavity	Hybrid GaAs GS	10	5	11.1	-	-
[21]	2*	No	Yes-IO	SIW	Hybrid GaAs GS	10	5	9	-	-
This work	2*	Yes‡	Yes-IO	Microstrip (Input) Ceramic Coax. (Output)	Hybrid GaN PA	4.7	9	15	36	55
This work	2*	Yes‡	Yes-O	Microstrip On-chip	MMIC GaAs PA	28	5	8	23	30

allowing the n th order filters, whereas others only show only second- or third-order cases. References [8] and [32] and do not have complex filter terminations, but rather use a transmission line section to transform the impedance to a real value. Chen *et al.* [16], [17] employed second- or third-order main-line filter topologies and used evanescent-mode cavity resonators for output matching at 3 GHz. Guo *et al.* [18] presented an output second-order matching filter with source-to-load coupling at 2.4 GHz. Work described in [19] and [20] shows X-band filters using large rectangular waveguide cavities with conjugate matching of the transistors. An extension to substrate-integrated waveguide (SIW) cavity filters with a feedback in the transistor is shown in [21], including also a method to estimate the noise figure from the coupling matrix. The work presented in this article demonstrates the first MMIC integrated FPA and the highest frequency implementation.

The theory is general and applies to both input and output complex-impedance filter matching networks, showing that reduced size and loss can be achieved by filter-amplifier code-sign. Implementing the FPA using heterogeneous integration could result in further miniaturization and reduced loss. The theory and experimental validation presented here is shown for narrowband transmitter PAs with the goal of filtering out-of-band spectral content. An interesting extension of this work to broadband transmitters should include the frequency-dependent active device impedance and is a topic of future research.

APPENDIX

REFLECTION COEFFICIENT EQUIVALENCE

Given a normalized impedance $z_0(f)$, the reflection coefficient is

$$\Gamma_0(f) = \frac{z_0(f) - 1}{z_0(f) + 1}. \quad (31)$$

This reflection coefficient is equal to that of another normalized impedance $z_f(f) = z_0(f) + jx$ for a source impedance $z_S = 1 - jx$. To prove this, we express the new reflection coefficient as [33]

$$\Gamma_f(f) = \frac{z_f(f) - z_S^*}{z_f(f) + z_S} \quad (32)$$

and substituting the impedance values, we obtain

$$\begin{aligned} \Gamma_f(f) &= \frac{[z_0(f) + jx] - (1 - jx)^*}{[z_0(f) + jx] + (1 - jx)} \\ &= \frac{z_0(f) - 1}{z_0(f) + 1} = \Gamma_0(f). \end{aligned} \quad (33)$$

ACKNOWLEDGMENT

The authors would like to thank WIN Semiconductor for monolithic microwave integrated circuit (MMIC) fabrication as a part of the ECEN 5014 class at the University of Colorado at Boulder taught by Zoya Popović. They would also like to thank Shane Verploegh for fabrication help. José R. Montejó-Garai acknowledges the Spanish Government programs (ADDMATE) TEC2016-76070-C3-2-R (AEI/FEDER/UE) and Fulbright-MICINN FMECD-ST-2019. Pedro de Paco thanks the Salvador de Madariaga Programme under Grant RTI2018-096019-B-C33. Zoya Popović was supported by the Lockheed Marting Endowed Chair of RF Engineering at the University of Colorado.

REFERENCES

- [1] S. Cripps, *RF Power Amplifiers for Wireless Communications*. Norwood, MA, USA: Artech House, 2006.
- [2] J. Wood, *Behavioral Modeling and Linearization of RF Power Amplifiers*. Norwood, MA, USA: Artech House, 2014.
- [3] C. Yu, N. Yang, Q. Lu, J. Cai, and X.-W. Zhu, "High-precision joint in-band/out-of-band distortion compensation scheme for wideband RF power amplifier linearization," *IEEE Microw. Wireless Compon. Lett.*, vol. 28, no. 11, pp. 1044–1046, Nov. 2018.
- [4] J. Chani-Cahuana, P. N. Landin, C. Fager, and T. Eriksson, "Iterative learning control for RF power amplifier linearization," *IEEE Trans. Microw. Theory Techn.*, vol. 64, no. 9, pp. 2778–2789, Sep. 2016.
- [5] R. N. Braithwaite, "Using a cascade of digital and analog predistortion to linearize a dual-band RF transmitter," in *Proc. IEEE Topical Conf. RF/Microwave Power Model. for Radio Wireless Appl. (PAWR)*, Jan. 2017, pp. 77–80.
- [6] J. Xia, A. Islam, H. Huang, and S. Boumaiza, "Envelope memory polynomial reformulation for hardware optimization of analog-RF predistortion," *IEEE Microw. Wireless Compon. Lett.*, vol. 25, no. 6, pp. 415–417, Jun. 2015.
- [7] C. Yu, L. Guan, E. Zhu, and A. Zhu, "Band-limited volterra series-based digital predistortion for wideband RF power amplifiers," *IEEE Trans. Microw. Theory Techn.*, vol. 60, no. 12, pp. 4198–4208, 2012.
- [8] X. Qi and F. Xiao, "Filtering power amplifier with up to 4th harmonic suppression," *IEEE Access*, vol. 8, pp. 29021–29026, 2020.

- [9] A. Sahu, P. H. Aaen, and V. K. Devabhaktuni, "Advanced technologies for next generation RF front end modules," *Int. J. RF Microw. Comput.-Aided Eng.*, vol. 29, no. 6, Jun. 2019, Art. no. e21700.
- [10] A. Suarez, F. Ramirez, and S. Sancho, "Stability analysis of power amplifiers under output mismatch effects," *IEEE Trans. Microw. Theory Techn.*, vol. 62, no. 10, pp. 2273–2289, Oct. 2014.
- [11] J. J. Carr, *The Technician's Radio Receiver Handbook*. Burlington, MA, USA: Newnes, 2000.
- [12] M. M. Ebrahimi, M. Helaoui, and F. M. Ghannouchi, "Minimizing matching network loss in output harmonic matched power amplifiers using harmonic load-pull measurement," in *Proc. IEEE Topical Conf. Power Model. Wireless Radio Appl.*, Jan. 2012, pp. 61–64.
- [13] M. Iwaki, J. Tsutsumi, M. Ueda, and Y. Satoh, "Co-design of SAW duplexer and LNA in RF transceiver IC for reducing total noise figure in RF front-end of cellular systems," in *Proc. IEEE Int. Ultrason. Symp.*, Sep. 2014, pp. 73–76.
- [14] C. Yoo, U. Kim, Y. Kwon, and J. Kim, "Helix on pad-type ultra small-size power amplifiers for WCDMA handset applications," *IEEE Microw. Wireless Compon. Lett.*, vol. 19, no. 12, pp. 825–827, Dec. 2009.
- [15] R. N. Simons, E. G. Wintucky, J. D. Wilson, and D. A. Force, "Ultra-high power and efficiency space traveling-wave tube amplifier power combiner with reduced size and mass for NASA missions," *IEEE Trans. Microw. Theory Techn.*, vol. 57, no. 3, pp. 582–588, Mar. 2009.
- [16] K. Chen, J. Lee, W. J. Chappell, and D. Peroulis, "Co-design of highly efficient power amplifier and high- Q output bandpass filter," *IEEE Trans. Microw. Theory Techn.*, vol. 61, no. 11, pp. 3940–3950, Nov. 2013.
- [17] K. Chen, T.-C. Lee, and D. Peroulis, "Co-design of multi-band high-efficiency power amplifier and three-pole high- Q tunable filter," *IEEE Microw. Wireless Compon. Lett.*, vol. 23, no. 12, pp. 647–649, Dec. 2013.
- [18] Q.-Y. Guo, X. Y. Zhang, J.-X. Xu, Y. C. Li, and Q. Xue, "Bandpass class-F power amplifier based on multifunction hybrid cavity–microstrip filter," *IEEE Trans. Circuits Syst. II, Exp. Briefs*, vol. 64, no. 7, pp. 742–746, Jul. 2017.
- [19] Y. Gao, J. Powell, X. Shang, and M. J. Lancaster, "Coupling matrix-based design of waveguide filter amplifiers," *IEEE Trans. Microw. Theory Techn.*, vol. 66, no. 12, pp. 5300–5309, Dec. 2018.
- [20] Y. Gao, X. Shang, C. Guo, J. Powell, Y. Wang, and M. J. Lancaster, "Integrated waveguide filter amplifier using the coupling matrix technique," *IEEE Microw. Wireless Compon. Lett.*, vol. 29, no. 4, pp. 267–269, Apr. 2019.
- [21] Y. Gao *et al.*, "Substrate integrated waveguide filter-amplifier design using active coupling matrix technique," *IEEE Trans. Microw. Theory Techn.*, vol. 68, no. 5, pp. 1706–1716, May 2020.
- [22] A. Atia, A. Williams, and R. Newcomb, "Narrow-band multiple-coupled cavity synthesis," *IEEE Trans. Circuits Syst.*, vol. CS-21, no. 5, pp. 649–655, Sep. 1974.
- [23] A. Atia and A. Williams, "New types of waveguide bandpass filters for satellite transponders," *Comsat Tech. Rev.*, vol. 1, no. 1, pp. 20–43, 1971.
- [24] A. E. Atia and A. E. Williams, "Narrow-bandpass waveguide filters," *IEEE Trans. Microw. Theory Techn.*, vol. MTT-20, no. 4, pp. 258–265, Apr. 1972.
- [25] A. E. Atia and A. E. Williams, "Nonminimum-phase optimum-amplitude bandpass waveguide filters," *IEEE Trans. Microw. Theory Techn.*, vol. 22, no. 4, pp. 425–431, Apr. 1974.
- [26] R. Cameron, C. Kudsia, and R. Mansour, *Microwave Filters for Communication System*. Hoboken, NJ, USA: Wiley, 2015.
- [27] J. Hong and M. Lancaster, *Microstrip Filters for RF/Microwave Applications*. Hoboken, NJ, USA: Wiley, 2004.
- [28] *Technical Specification Group Services and System Aspects; Release 15 Description; Summary of Rel-15 Work Items (Release 15)*, document 315, 3rd Generation Partnership Project Std, Sep. 2019.
- [29] P. Bell, Z. Popovic, and C. W. Dyck, "MEMS-switched class-A-to-E reconfigurable power amplifier," in *Proc. IEEE Radio Wireless Symp.*, Oct. 2006, pp. 243–246.
- [30] M. Roberg and Z. Popovic, "Analysis of high-efficiency power amplifiers with arbitrary output harmonic terminations," *IEEE Trans. Microw. Theory Techn.*, vol. 59, no. 8, pp. 2037–2048, Aug. 2011.
- [31] T. Jensen, V. Zhurbenko, V. Krozer, and P. Meincke, "Coupled transmission lines as impedance transformer," *IEEE Trans. Microw. Theory Techn.*, vol. 55, no. 12, pp. 2957–2965, Dec. 2007.
- [32] Y. C. Li, K. C. Wu, and Q. Xue, "Power amplifier integrated with bandpass filter for long term evolution application," *IEEE Microw. Wireless Compon. Lett.*, vol. 23, no. 8, pp. 424–426, Aug. 2013.

- [33] K. Kurokawa, "Power waves and the scattering matrix," *IEEE Trans. Microw. Theory Techn.*, vol. 13, no. 2, pp. 194–202, Mar. 1965.



José Antonio Estrada (Member, IEEE) received the B.S. degree in electrical engineering from the University of Carabobo, Valencia, Venezuela, in 2012, and the M.S. degree in electrical engineering from the University of Colorado at Boulder, Boulder, CO, USA, in 2017, where he is currently pursuing the Ph.D. degree in electrical engineering.

He was an Assistant Lecturer with the University of Carabobo from 2012 to 2015 and a Researcher with the Applied Electromagnetics Laboratory, Fundación Instituto de Ingeniería, Caracas, Venezuela, from 2014 to 2015, working as a Laboratory Coordinator, leading research projects and overseeing EMC compliance and antenna testing. His research interests include the design of high-efficiency power amplifiers, microwave filters, tuneable RF front ends, front-end miniaturization, heterogeneous integration, energy harvesting, and wireless powering.



José R. Montejo-Garai was born in Vitoria-Gasteiz, Spain, in 1965. He received the Ingeniero de Telecomunicación and Ph.D. degrees from the Universidad Politécnica de Madrid, Madrid, Spain, in 1990 and 1994, respectively.

Since 1989, he has been with the Grupo de Electromagnetismo Aplicado y Microondas, Universidad Politécnica de Madrid, as an Assistant Professor, until 1996, and as an Associate Professor, until 2017, where he is currently a Full Professor. His current research interests include the analysis and characterization of waveguide structures, advanced synthesis theory, and computer-aided design for microwave and millimeter-wave passive devices: filters, multiplexers, orthomode transducers, and beam-forming networks. He has designed plenty of passive microwave devices for communication satellites.



Pedro de Paco (Member, IEEE) was born in Badalona, Spain. He received the M.S. degree in telecommunication engineering and the Ph.D. degree (*cum laude*) from the Universitat Politècnica de Catalunya (UPC), Barcelona, Spain, in 1997 and 2003, respectively.

In 1998, he joined the Electromagnetic and Photonics Engineering Group (EEF), Signal Theory and Communications Department (TSC-UPC), with a grant from the Institut d'Estudis Espacials de Catalunya (IEEC) in a joint activity related with the European scientific space mission Planck. He was a member of the LFI-Radiometer working group and the Planck Consortium. During his Ph.D. and UPC stage, he has participated in several national and international research projects mostly related to microwave and millimeter-wave circuits and systems applied to design and testing of remote sensing instruments and front-endpoint-to-multipoint broadband communication system. Since 2004, he has been an Associate Professor with the Universitat Autònoma de Barcelona (UAB), Barcelona, where he teaches applied electromagnetics and microwave engineering courses. From 2010 to 2013, he was the Deputy Director and a member of the Executive Board of the Telecommunication and System Engineering Department, UAB. From 2018 to 2019, he was a Visiting Researcher with the Microwave and RF Research Group, University of Colorado at Boulder, Boulder, CO, USA. His main research interests include microwave filter synthesis and microwave acoustics filter synthesis and design, as well as microwave and radar systems and devices.

Dr. de Paco Sánchez was awarded three times with merits in research and recognized with merits in University training by l'Agència de Qualitat and awarded with Advanced Research by Generalitat Catalunya. He has advised eight Ph.D. students. He has been appointed as a Technical Expert for the Telecommunications Equipment by the National Agency of Accreditation. He is a member of the MTT-6 RF MEMS and Microwave Acoustics Committee and a Reviewer of the IEEE TRANSACTIONS ON MICROWAVE THEORY AND TECHNIQUES and the IEEE MICROWAVE AND WIRELESS COMPONENTS LETTERS. He serves as a member of the Technical Review Board for the European Microwave Conference.



Dimitra Psychogiou (Senior Member, IEEE) received the Dipl.Eng. degree in electrical and computer engineering from the University of Patras, Patras, Greece, in 2008, and the Ph.D. degree in electrical engineering from the Swiss Federal Institute of Technology (ETH), Zürich, Switzerland, in 2013.

From 2013 to 2016, she was with Purdue University, West Lafayette, IN, USA. She is currently an Assistant Professor of electrical, computer and energy engineering with the University of Colorado at Boulder (UC Boulder), Boulder, CO, USA. Her

research has been presented in more than 160 IEEE publications. Her current research interests include RF design and characterization of reconfigurable microwave and millimeter-wave passive components, RF-MEMS, acoustic wave resonator-based filters, tunable filter synthesis, and frequency-agile antennas.

Dr. Psychogiou is a Senior Member of URSI and an elected member of the IEEE MTT-S Filters and Passive Components (MTT-5) Technical Committee and the IEEE MTT-S Microwave Control Materials and Devices (MTT-13) Committee, where she is currently serving as the Vice-Chair. She received the 2020 CAREER Award from the National Science Foundation (NSF), the 2020 URSI Young Scientist Award, and the Junior Faculty Outstanding Research Award from UC Boulder. She is also an Associate Editor of the IEEE MICROWAVE AND WIRELESS COMPONENTS LETTERS and *IET Microwaves, Antennas, and Propagation* and serves on the Technical Review Board for various the IEEE and EuMA conferences and journals. She is also the Secretary of the USNC-URSI Commission D.



Zoya Popović (Fellow, IEEE) received the Dipl.Eng. degree from the University of Belgrade, Belgrade, Serbia, in 1985, and the Ph.D. degree from Caltech, Pasadena, CA, USA, in 1990.

She was a Visiting Professor with the Technical University of Munich, Munich, Germany, from 2001 to 2003, and ISAE, Toulouse, France, in 2014, and the Chair of Excellence at Carlos III University, Madrid, Spain, from 2018 to 2019. She is currently a Distinguished Professor and the Lockheed Martin Endowed Chair of electrical engineering with

the University of Colorado at Boulder, Boulder, CO, USA. Her research interests are in high-efficiency power amplifiers and transmitters, microwave and millimeter-wave high-performance circuits for communications and radar, medical applications of microwaves, millimeter-wave and terahertz quasi-optical techniques, and wireless powering.

Dr. Popović was elected as a Foreign Member of the Serbian Academy of Sciences and Arts in 2006. She was a recipient of two IEEE MTT Microwave Prizes for best journal articles, the White House NSF Presidential Faculty Fellow Award, the URSI Issac Koga Gold Medal, the ASEE/HP Terman Medal, and the German Humboldt Research Award. She has graduated over 60 Ph.D. students and currently advises 11 doctoral students. She was named the IEEE MTT Distinguished Educator in 2013 and the University of Colorado Distinguished Research Lecturer in 2015.